Scripta Materialia 224 (2023) 115043

Contents lists available at ScienceDirect

Scripta Materialia

journal homepage: www.journals.elsevier.com/scripta-materialia

Improvement of resistance against hydrogen embrittlement by controlling carbon segregation at prior austenite grain boundary in 3Mn-0.2C martensitic steels

Kazuho Okada [a,b,*], Akinobu Shibata [a,c], Taisuke Sasaki [c,d], Hisashi Matsumiya [b], Kazuhiro Hono [d], Nobuhiro Tsuji [b,c]

[a] Research Center for Structural Materials, National Institute for Materials Science (NIMS), 1-2-1 Sengen, Tsukuba 305-0047, Japan
[b] Department of Materials Science and Engineering, Kyoto University, Yoshida-honmachi, Kyoto, Sakyo-ku 606-8501, Japan
[c] Elements Strategy Initiative for Structural Materials (ESISM), Kyoto University, Yoshida-honmachi, Kyoto, Sakyo-ku 606-8501, Japan
[d] Research Center for Magnetic and Spintronic Materials, National Institute for Materials Science (NIMS), 1-2-1 Sengen, Tsukuba 305-0047, Japan

ARTICLE INFO

Keywords:
Hydrogen embrittlement
Grain boundary embrittlement
Martensitic steel
Atom probe tomography
Grain boundary segregation

ABSTRACT

This study challenged to improve the resistance against hydrogen embrittlement by increasing the concentration of carbon segregated at prior austenite grain boundary (PAGB), X_{PAGB}, in low-carbon martensitic steels. The specimens with/without carbon segregation treatment (Non-seg and Seg specimens, respectively) had almost the same microstructure, other than higher X_{PAGB} in the Seg specimen. While the uncharged Non-seg and Seg specimens exhibited similar mechanical properties, the maximum stress of the hydrogen-charged specimen was much higher in the Seg specimen than that in the Non-seg specimen even when diffusible hydrogen contents were almost the same. In addition, the fraction of intergranular fracture surface was much smaller in the Seg specimen. Based on these results, we conclude that the segregated carbon suppressed the accumulation of hydrogen around PAGB by site competition and increased cohesive energy of PAGB, leading to the significantly improved resistance against hydrogen-related intergranular fracture.

High-strength steels, such as martensitic steels, have been used in various industrial applications. However, high-strength martensitic steels are highly susceptible to hydrogen embrittlement which is the phenomenon that hydrogen degrades the mechanical properties of metals and alloys [1,2]. Since a certain amount of hydrogen is inevitably introduced into martensitic steels during the manufacturing process and in use, it is desirable to improve their resistance against hydrogen embrittlement.

Lath martensite is a typical microstructure of low- and medium-carbon high-strength steels. A lath martensitic structure consists of several structural units with different size scales, namely, lath, block, packet, and prior austenite grain (PAG) [3–5]. A lath is a single crystal of martensite whose thickness is below 1 μm. A block is composed of many laths having nearly identical crystallographic orientations, and a packet consists of several blocks having nearly the same habit plane orientations. Due to these structural units, martensitic structure contains several types of high-angle boundaries, such as block boundaries, packet boundaries, in addition to PAG boundaries (PAGB). On the other hand, the lath boundaries are low-angle boundaries whose misorientation is less than 5° [6]. Intergranular fracture is one of the typical hydrogen-related fracture modes. Although martensitic structure contains several types of high-angle boundaries, the hydrogen-related intergranular fracture occurs mainly along PAGB [7–10]. This could be due to the hydrogen accumulation around PAGB during deformation [11–14]. Recently, first-principles calculations [15–17], molecular statics simulations [18], and molecular dynamics simulations [19] have revealed that hydrogen reduces the cohesive energy of grain boundaries (γ_{GB}) in iron. Yamaguchi and Kameda [20] performed first-principles calculations for γ_{GB} at Σ3(111) grain boundary in iron and revealed that carbon segregation suppressed the reduction of γ_{GB} by hydrogen. However, it has not yet been verified whether carbon segregation at PAGB is effective or not in reducing susceptibility to hydrogen embrittlement in martensitic steels. The present study experimentally demonstrates that the resistance against hydrogen embrittlement in

* Corresponding author.
E-mail addresses: okada.kazuho@nims.go.jp (K. Okada), shibata.akinobu@nims.go.jp (A. Shibata), sasaki.taisuke@nims.go.jp (T. Sasaki), matsumiya.hisashi.42a@st.kyoto-u.ac.jp (H. Matsumiya), kazuhiro.hono@nims.go.jp (K. Hono), nobuhiro-tsuji@mtl.kyoto-u.ac.jp (N. Tsuji).

https://doi.org/10.1016/j.scriptamat.2022.115043
Received 19 July 2022; Received in revised form 26 August 2022; Accepted 7 September 2022
Available online 3 November 2022

martensitic steels can be improved by increasing carbon segregation at PAGB.

An Fe-3Mn-0.2C (Mn: 3.02, C: 0.18, Si: 0.01, $P < 0.002$, S: 0.001, Al: 0.002, N: 0.002, O: 0.001, and Fe: bal. (wt.%)) alloy was used in the present study. The as-cast ingot was cold-rolled from 15 to 1.5 mm in thickness and heat-treated in two different ways as schematically shown in Fig. 1(a). One is one-step austenitization; the specimen was austenitized at 1100 °C for 30 min in a vacuum, followed by ice-brine quenching and sub-zero cooling in liquid nitrogen. The other is two-step austenitization; the specimen was held at 790 °C (just above A_3) for 30 min following the austenitization (1100 °C, 30 min), and then ice-brine quenched and sub-zero cooled in liquid nitrogen. The isothermal-holding at 790 °C aimed at increasing carbon segregation at (prior) austenite grain boundaries. Hereafter, we refer to the specimens with one-step and two-step austenitizations as the "Non-seg specimen" and the "Seg specimen", respectively. According to McLean's equation [21], it is expected that the concentration of segregated carbon at PAGB (X_{PAGB}) increases during the isothermal-holding at 790 °C:

$$\frac{X_{GB}}{1-X_{GB}} = \frac{X_m}{1-X_m} exp\left(\frac{-\Delta G}{RT}\right), \quad (1)$$

where X_{GB} is atomic fraction of carbon at austenite grain boundaries, X_m is atomic fraction of carbon in matrix, ΔG is segregation energy, R is gas constant (= 8.31 J $K^{-1}mol^{-1}$), and T is temperature. Paju and Grabke [22] measured X_{PAGB} by Auger electron spectroscopy and reported that the value of ΔG was -0.31 eV. Assuming that ΔG = -0.31 eV in the present steel, X_{PAGB} in the Seg specimen is expected to be more than two times higher than that in the Non-seg specimen. Previous studies confirmed X_{PAGB} increased with decreasing isothermal-holding temperature in the austenite region using Auger electron spectroscopy [23] and three-dimensional atom probe (3DAP) [24].

The microstructures were characterized using optical microscopy (OM, OLYMPUS: DSX1000), scanning electron microscopy (SEM, JEOL: JSM-7800F), electron backscattering diffraction in SEM (EBSD, JEOL: JSM-7100F), and scanning transmission electron microscopy (STEM, JEOL: JEM-2100F). X_{PAGB} was evaluated by direct measurements of carbon concentration using 3DAP (CAMECA, LEAP5000XS). Needle-shaped specimens for the 3DAP analysis were lifted out from PAGB using focused ion-beam/SEM (FIB/SEM) (Thermo Fisher Scientific, Helios 5 DualBeam). The temperature, laser pulse energy, pulse rate, and pulse fraction for the 3DAP analysis were 50 K, 50 pJ, 250 kHz, and 0.5%, respectively. Sheet-type tensile test specimens with a gage length of 10 mm, a width of 5 mm, and a thickness of 1 mm were cathodically pre-charged with hydrogen in an aqueous solution of 3% NaCl + 3 gL^{-1} NH_4SCN for 24 h at current densities of 0.5 and 1.0 Am^{-2}. Uniaxial tensile tests were then performed at a strain rate of 8.3×10^{-6} s^{-1} at ambient temperature in air. The diffusible hydrogen content (H_D) was

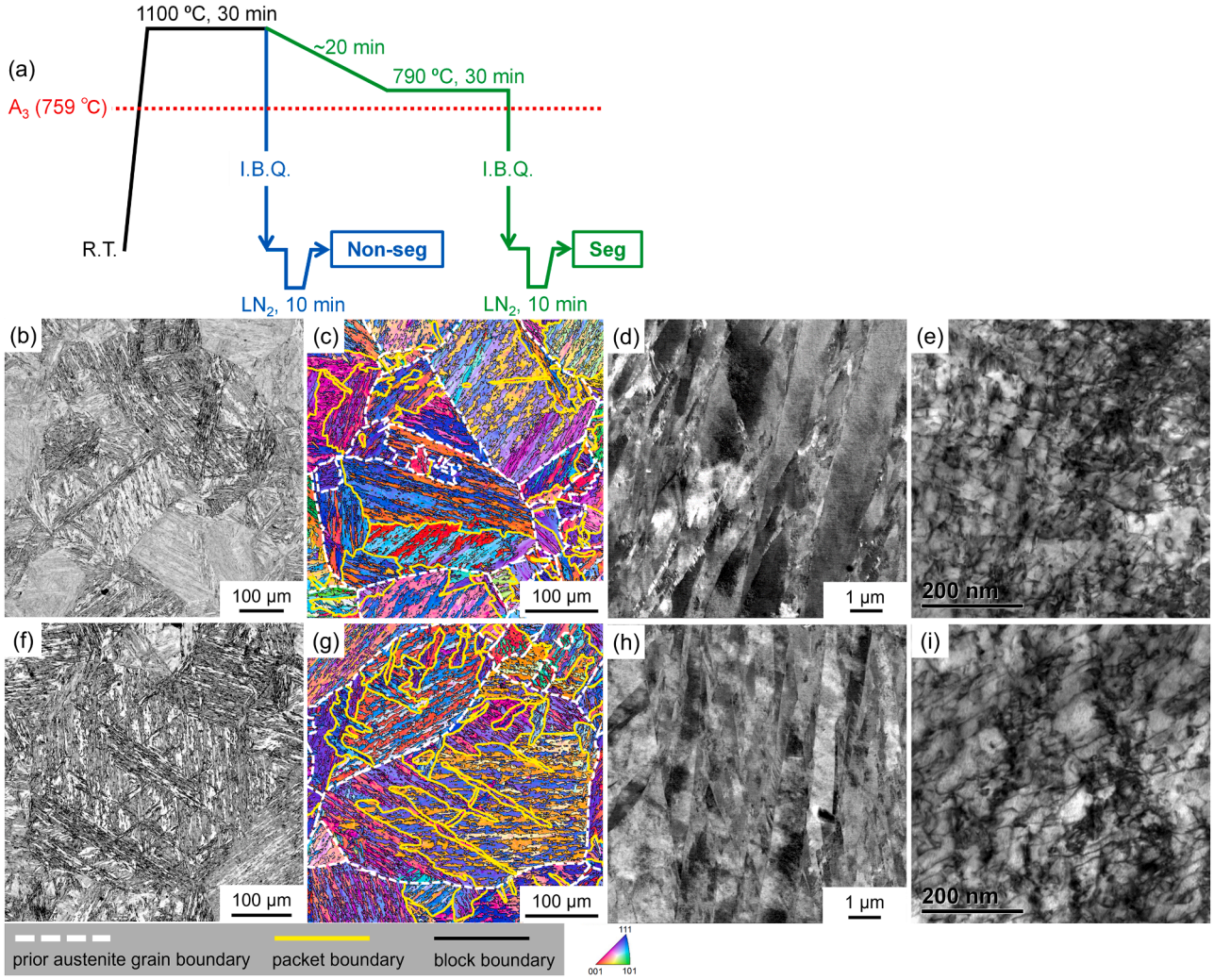

Fig. 1. (a) Schematic illustration of the heat treatments. (b,f) OM images, (c,g) EBSD orientation maps, (d,h) SEM-BSE images, and (e,i) STEM images of the lath martensitic microstructures after the heat treatments ((b–e) Non-seg specimen and (f–i) Seg specimen). The white broken lines, yellow solid lines, and black solid lines in (c,g) indicate the positions of prior austenite grain boundaries, packet boundaries, and block boundaries, respectively.

measured by thermal desorption spectroscopy (TDS) at a heating rate of 100 °C/h using J-SCIENCE LAB CO. Ltd.: JTF-20A. The tensile tests and TDS measurements were started always 40 min after the completion of pre-charging. These tests and measurements were performed three times for each condition to ensure reproducibility.

Fig. 1(b–i) shows the microstructures of (b–e) the Non-seg specimen and (f–i) the Seg specimen; (b,f) OM images, (c,g) EBSD orientation maps, (d,h) SEM-backscattered electron (BSE) images, and (e,i) STEM images. Both specimens had fully martensitic microstructure. As summarized in Table 1, the average widths (W) or diameters (D) of lath (W_{lath}), block (W_{block}), packet (D_{packet}), and PAG (D_{PAG}) were almost the same between the Non-seg and Seg specimens. X-ray diffraction experiments were performed using BL46XU in SPring-8 and the dislocation densities were evaluated by a convolutional multiple whole profile (CMWP) fitting [25–27]. The dislocation densities (ρ) of the Non-seg and Seg specimens were $7.89 \pm 0.71 \times 10^{15}$ m^{-2} and $7.57 \pm 0.26 \times 10^{15}$ m^{-2}, respectively, nearly the same values (Table 1). In addition, as shown in the STEM images of Fig. 1(e,i), we could not find any apparent difference between the dislocation morphologies.

Miyamoto et al. [24] evaluated the concentration of segregated boron at PAGB using 3DAP, and reported that the concentration increased with increasing misorientation of parent austenite grain boundary (θ_{parent}) up to 30° and then became constant with further increase of θ_{parent}. The misorientation-dependent segregation of carbon is also expected to occur because carbon is an interstitial element in iron like boron. Moreover, carbon segregation at lath boundaries and dislocations were also reported [28–30]. Morsdorf et al. [28] calculated the diffusion distance of carbon during martensitic transformation and reported that carbon atoms can diffuse ~6 μm between M_s (~423 °C) and M_f (~179 °C) when the cooling rate is -100 °C/s. Herbig et al. [31] reported that carbon segregation at random ferrite grain boundaries increased with increasing misorientation up to 14° and became constant with further increase of the misorientation. Therefore, carbon diffusion during quenching also leads to carbon segregation depending on the misorientation of PAGB (θ_{prior}). Hence, in order to eliminate the effect of misorientation-dependent carbon segregation, we compared X_{PAGB} whose θ_{parent} and θ_{prior} were larger than 30°, which were measured from EBSD orientation data. We analyzed two needles of 3DAP specimens for each of the Non-seg specimen (A and B) and the Seg specimen (C and D). Fig. 2 shows 3DAP results of (a,b,e) the Non-seg specimen (B) and (c,d,f) the Seg specimen (D); (a,c) bright-field TEM images of the 3DAP specimens, (b,d) 3D carbon distribution maps, and (e,f) corresponding concentration profiles of manganese and carbon across the PAGB. The concentration profiles were obtained along the longitudinal direction of selected volumes ($20 \times 20 \times 50$ nm^3) indicated by blue in Fig. 2(b,d). The peak concentration of carbon was higher in the Seg specimen (D) (5.84 at.%) than that in the Non-seg specimen (B) (3.62 at.%), while there was no significant manganese segregation at the PAGB in either specimen. We quantified X_{PAGB} using ladder diagram plot [32,33], and the average X_{PAGB} obtained from voluntary four selected volumes in each specimen was summarized in Fig. 2(g). The X_{PAGB} in the Seg specimens (C: 4.50 at.% and D: 4.65 at.%) were much higher than those in the Non-seg specimens (A: 2.71 at.% and B: 3.10 at.%). We note that elements other than iron, manganese, and carbon were not detected in the 3DAP analysis. According to Wells et al. [34], carbon atoms can diffuse 112.2 μm at 847 °C in a 0.22 wt.% C steel. The diffusion distance is larger than PAG radius (Non-seg: 91.5 μm, Seg: 93.5 μm), so that carbon atoms can well diffuse to the PAGB during isothermal-holdings in the austenite region (Non-seg: 1100 °C, Seg: 790 °C). From our 3DAP result (Fig. 2(g)), we can obtain the value of ΔG as -0.156 eV for the present steel (0.18 wt.% C) in McLean's equation (Eq. (1)). The difference between carbon concentrations measured by 3DAP (whole needle average) and by infrared absorption method (bulk average) was smaller than 2%.

Fig. 3 shows (a) hydrogen desorption profiles and (b) H_D in the hydrogen-charged specimens obtained by TDS. Solid and broken lines in Fig. 3(a) indicate the results for current densities of 0.5 Am^{-2} and 1.0 Am^{-2}, respectively. Both the uncharged Non-seg and Seg specimens did not contain diffusible hydrogen ($H_D = 0.0$ wt. ppm). The H_D at current densities of 0.5 Am^{-2} and 1.0 Am^{-2} were 0.477 wt. ppm and 0.886 wt. ppm in the Non-seg specimen (blue), respectively, which were nearly the same as those in the Seg specimen (green) (0.5 Am^{-2}: 0.489 wt. ppm, 1.0 Am^{-2}: 0.811 wt. ppm). In addition, as shown in Fig. 3(a), the Non-seg and Seg specimens exhibited similar shapes of the desorption profiles, suggesting that hydrogen trapping sites in these specimens were almost the same.

Fig. 4(a) shows nominal stress – nominal strain curves of the Non-seg specimens (blue) and the Seg specimens (green) obtained by tensile tests. In the uncharged specimens (solid lines), there were no significant differences in the ultimate tensile strength and the total elongation between the Non-seg and Seg specimens. In contrast, in the hydrogen-charged specimens (0.5 Am^{-2}: broken lines, 1.0 Am^{-2}: chain lines), the maximum stresses were higher in the Seg specimens than those in the Non-seg specimens though H_D were similar values. The average maximum stress of each condition was summarized in Fig. 4(b). It is evident that hydrogen-induced degradation of the mechanical property was notably suppressed in the Seg specimen. In particular, at a current density of 0.5 Am^{-2}, the maximum stress was higher than the 0.2% proof stress ($\sigma_{0.2}$, 1032 MPa) (a green broken line) in the Seg specimen, while the Non-seg specimen was prematurely fractured in the elastic strain region. We note that $\sigma_{0.2}$ was obtained from the uncharged specimen because some of the hydrogen-charged specimens were fractured in the elastic strain region.

Fig. 5 shows SEM images of the fracture surfaces in the hydrogen-charged (a–d) Non-seg specimen and (e–h) Seg specimen at a current density of 0.5 Am^{-2} ((a,e) ductile fracture surfaces with dimple pattern, (b,f) cleavage fracture surfaces, (c,g) intergranular fracture surfaces, and (d,h) quasi-cleavage fracture surfaces). Because cleavage and quasi-cleavage surfaces are characterized by river patterns and serrated markings, respectively [8], we can distinguish them from a morphological perspective. These fracture surface morphologies were also observed in other conditions and the area fractions of these morphologies were summarized in Fig. 5(i–k). In the uncharged specimen (Fig. 5 (i)), the fracture surfaces were mainly composed of ductile fracture surface (red) in both specimens, and cleavage fracture surface (yellow) was observed only in the Non-seg specimen. In the hydrogen-charged specimens (Fig. 5(j) 0.5 Am^{-2} and (k) 1.0 Am^{-2}), intergranular fracture surface (blue) and quasi-cleavage fracture surface (green) were observed, suggesting the occurrence of hydrogen-related fracture. In both the Non-seg and Seg specimens, the fractions of intergranular fracture surface (f_{IG}) increased with increasing H_D. However, f_{IG} in the Seg specimens were 11.3% (0.5 Am^{-2}) and 63.6% (1.0 Am^{-2}), much

Table 1
Summary of the average widths (W) or diameters (D) of lath (W_{lath}), block (W_{block}), packet (D_{packet}), and prior austenite grain boundary (D_{PAG}), and the dislocation densities (ρ) in the Non-seg and Seg specimens.

	W_{lath}	W_{block}	D_{packet}	D_{PAG}	ρ
Non-seg	0.478 ± 0.030 μm	4.44 ± 0.26 μm	68.6 ± 2.3 μm	183 ± 9.5 μm	$7.89 \pm 0.71 \times 10^{15}$ m^{-2}
Seg	0.469 ± 0.035 μm	3.62 ± 0.15 μm	81.3 ± 3.1 μm	187 ± 10.0 μm	$7.57 \pm 0.26 \times 10^{15}$ m^{-2}

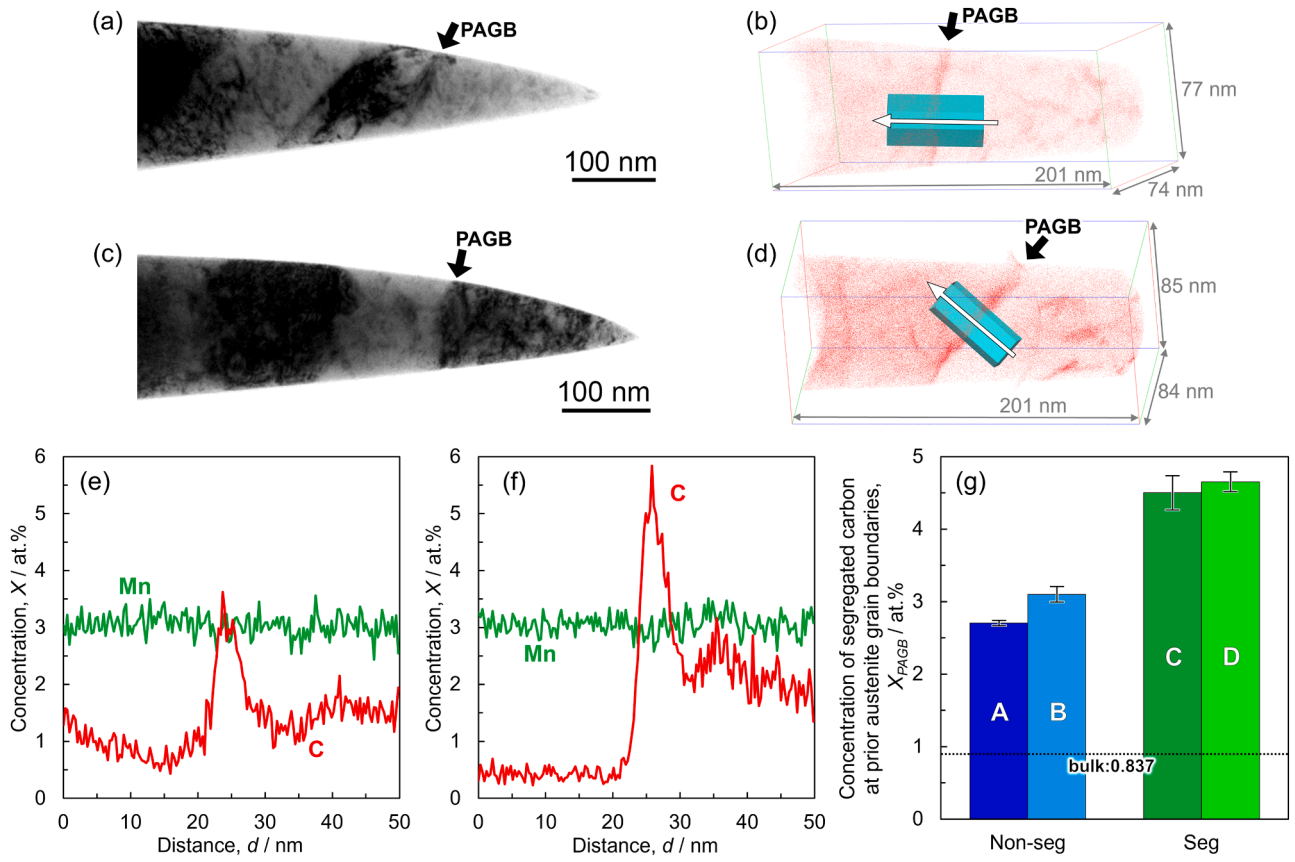

Fig. 2. (a,c) Bright-field TEM images of the 3DAP specimens, (b,d) 3D carbon distribution maps, and (e,f) corresponding concentration profiles of manganese and carbon across the PAGB ((a,b,e) Non-seg specimen (B) and (c,d,f) Seg specimen (D)). The size of selected volumes (indicated by blue) for obtaining concentration profiles is $20 \times 20 \times 50$ nm^3. (g) Concentration of segregated carbon at PAGB (X_{PAGB}) obtained by ladder diagram plot in each specimen.

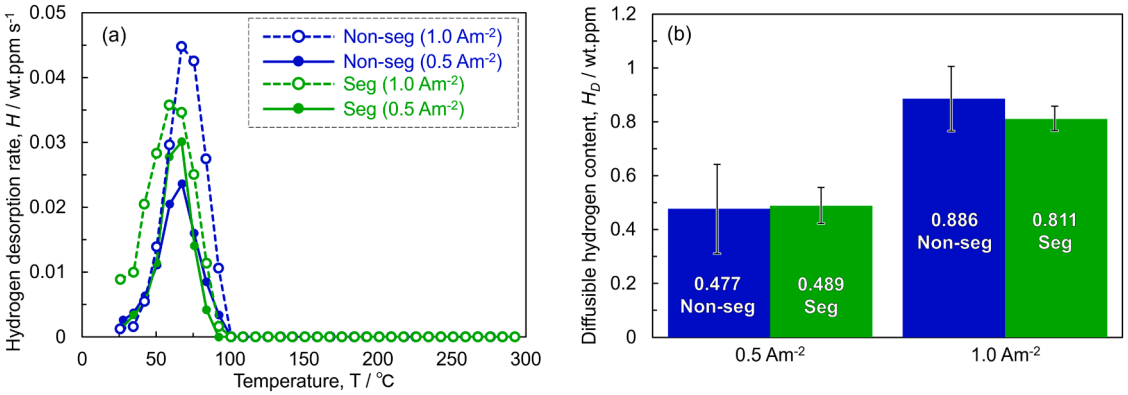

Fig. 3. (a) Hydrogen desorption profiles obtained by TDS. Solid and broken lines indicate 0.5 Am^{-2} and 1.0 Am^{-2}, respectively. (b) The diffusible hydrogen contents (H_D) at current densities of 0.5 Am^{-2} and 1.0 Am^{-2}. Blue and green indicate the Non-seg and Seg specimens, respectively.

smaller than those in the Non-seg specimens (0.5 Am^{-2}: 55.5%, 1.0 Am^{-2}: 82.3%). This strongly suggests that the hydrogen-related intergranular fracture was suppressed in the Seg specimen.

Without hydrogen, the mechanical properties of the Non-seg and Seg specimens were similar. On the other hand, although H_D was almost the same, the maximum stresses of the hydrogen-charged Seg specimens were much higher than those of the hydrogen-charged Non-seg specimens (Figs. 3 and 4). Although strength as well as susceptibility to hydrogen embrittlement were greatly affected by microstructure in martensitic steels, such as block size, PAG size, and dislocation density [35–37], a series of microstructure analysis has shown that there were no clear differences in the sizes of each structural unit and dislocation densities between the Non-seg and Seg specimens (Fig. 1 and Table 1). The 3DAP analysis clarified that X_{PAGB} was higher in the Seg specimen than that in the Non-seg specimen (Fig. 2). Based on the simple assumption that peak concentration of carbon and thickness of all the segregated area along PAGB are 5.84 at.% and 10 nm (Fig. 2), respectively, the decrease of average carbon concentration in matrix caused by carbon segregation at PAGB was negligibly small (smaller than 0.001 wt.%) in the Seg specimen. Therefore, we can conclude that the suppression of hydrogen embrittlement in the Seg specimen should be attributed to the carbon segregation at the PAGB. According to Yamaguchi and Kameda [20,38], carbon segregation at ferrite grain boundary has two effects on the resistance against hydrogen embrittlement. Firstly, the

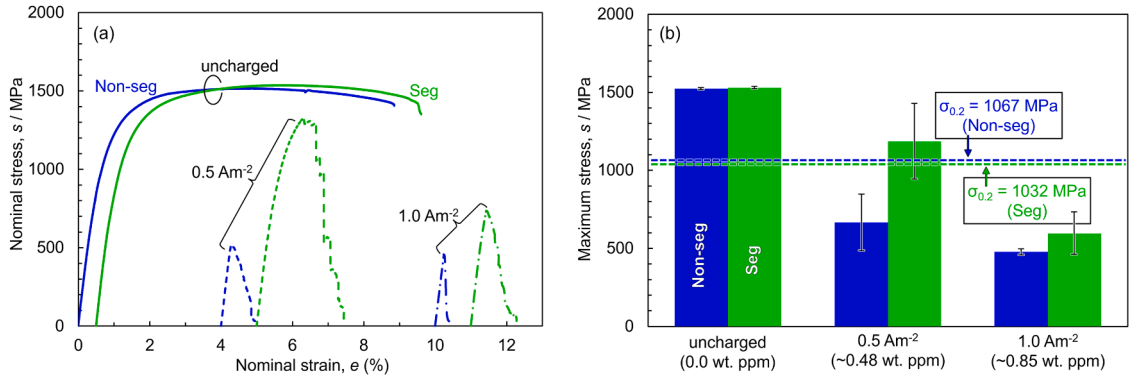

Fig. 4. (a) Nominal stress – nominal strain curves of the uncharged specimens (solid lines) and the hydrogen-charged specimens at current densities of 0.5 Am^{-2} (broken lines) and 1.0 Am^{-2} (chain lines). (b) Relationship between the maximum stress of tensile test and the current density. Broken lines in (b) indicate the 0.2% proof stresses (σ0.2) of the uncharged specimens. Blue and green indicate the Non-seg and Seg specimens, respectively.

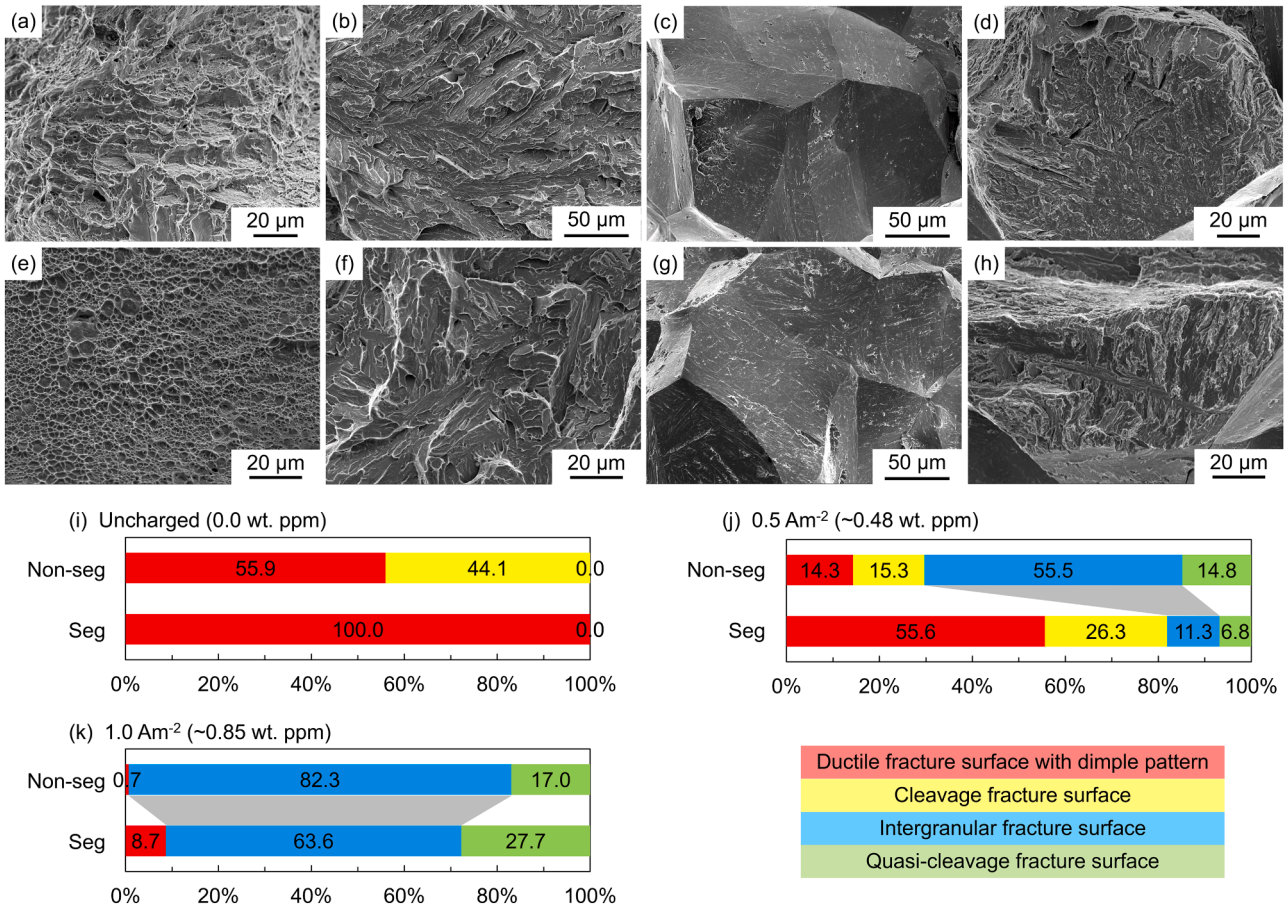

Fig. 5. SEM images showing fracture surfaces of the hydrogen-charged (a–d) Non-seg specimen and (e–f) Seg specimen at a current density of 0.5 Am^{-2}. Area fractions of the ductile fracture surface with dimple pattern (red), cleavage fracture surface (yellow), intergranular fracture surface (blue), and quasi-cleavage fracture surface (green) at current densities of (i) 0.0 Am^{-2} (uncharged), (j) 0.5 Am^{-2}, and (j) 1.0 Am^{-2}.

segregated carbon atoms increase γ_{GB}. Secondly, the segregated carbon atoms reduce the occupancy of hydrogen atoms at the grain boundary by site competition. They proposed that these effects led to the suppression of the reduction of γ_{GB} by hydrogen. It has been reported that hydrogen accumulated around PAGB during tensile deformation, while the accumulation was not clearly observed without deformation [13,14]. Hence, the reduction of PAGB cohesive energy (γ_{PAGB}) by accumulated hydrogen during deformation led to the intergranular fracture. We infer that, in the Seg specimen, high X_{PAGB} increased the γ_{PAGB} and suppressed the hydrogen accumulation around the PAGB by site competition. As a result, the hydrogen-related intergranular fracture was suppressed and the resistance against hydrogen embrittlement was improved.

To summarize, we experimentally demonstrated that increasing X_{PAGB} improved the resistance against hydrogen embrittlement in martensitic steels. The Non-seg and Seg specimens had similar microstructure, but only X_{PAGB} was higher in the Seg specimen. While the uncharged Non-seg and Seg specimens exhibited similar mechanical properties, the maximum stress of the hydrogen-charged specimen was much higher in the Seg specimen than that in the Non-seg specimen even when H_D were almost the same. In addition, the f_{IG} was much smaller in

the Seg specimen. Based on these results, we conclude that the segregated carbon suppressed the accumulation of hydrogen around PAGB by site competition and increased γ_{PAGB}, leading to the suppression of intergranular fracture and the resultant improvement of the resistance against hydrogen embrittlement.

Declaration of Competing Interest

The authors declare that they have no known competing financial interests or personal relationships that could have appeared to influence the work reported in this paper.

Acknowledgements

This study was financially supported by JSPS KAKENHI Grant Numbers JP19J21267, JP19H02459, and JP20K21083, and the Elements Strategy Initiative for Structural Materials (ESISM, No. JPMXP0112101000) through the Ministry of Education, Culture, Sports, Science and Technology (MEXT), Japan.

References

[1] J. Venezuela, Q. Liu, M. Zhang, Q. Zhou, A Atrens, A review of hydrogen embrittlement of martensitic advanced high-strength steels, Corros. Rev. 34 (2016) 153–186.
[2] M.L. Martin, M.J. Connolly, F.W. DelRio, A.J. Slifka, Hydrogen embrittlement in ferritic steels, Appl. Phys. Rev. 7 (2020), 041301.
[3] A.R. Marder, G. Krauss, The morphology of martensite in iron-carbon alloys, Trans. Am. Soc. Met. 60 (1967) 651–660.
[4] G. Krauss, A.R. Marder, The morphology of martensite in iron alloys, Metall. Trans. 2 (1971) 2343–2357.
[5] S. Morito, H. Tanaka, R. Konishi, T. Furuhara, T. Maki, The morphology and crystallography of lath martensite in Fe-C alloys, Acta Mater. 51 (2003) 1789–1799.
[6] S. Morito, X. Huang, T. Furuhara, T. Maki, N. Hansen, The morphology and crystallography of lath martensite in alloy steels, Acta Mater. 54 (2006) 5323–5331.
[7] M. Wang, E. Akiyama, K. Tsuzaki, Effect of hydrogen on the fracture behavior of high strength steel during slow strain rate test, Corros. Sci. 49 (2007) 4081–4097.
[8] A. Shibata, Y. Momotani, T. Murata, T. Matsuoka, M. Tsuboi, N. Tsuji, Microstructural and crystallographic features of hydrogen-related fracture in lath martensitic steels, Mater. Sci. Technol. 33 (2017) 1524–1532.
[9] A. Shibata, T. Murata, H. Takahashi, T. Matsuoka, N. Tsuji, Characterization of hydrogen-related fracture behavior in as-quenched low-carbon martensitic steel and tempered medium-carbon martensitic steel, Metall. Mater. Trans. A 46 (2015) 5685–5696.
[10] A. Shibata, Y. Madi, K. Okada, N. Tsuji, J. Besson, Mechanical and microstructural analysis on hydrogen-related fracture in a martensitic steel, Int. J. Hydrog. Energy 44 (2019) 29034–29046.
[11] J. Ovejero-Garcia, Hydrogen microprint technique in the study of hydrogen in steels, J. Mater. Sci. 20 (1985) 2623–2629.
[12] K. Takai, J. Seki, Y. Homma, Observation of trapping sites of hydrogen and deuterium in high-strength steels by using secondary ion mass spectrometry, Mater. Trans. 36 (1995) 1134–1139. JIM.
[13] Y. Momotani, A. Shibata, D. Terada, N. Tsuji, Effect of strain rate on hydrogen embrittlement in low-carbon martensitic steel, Int. J. Hydrog. Energy 42 (2017) 3371–3379.
[14] Y. Momotani, A. Shibata, T. Yonemura, Y. Bai, N. Tsuji, Effect of initial dislocation density on hydrogen accumulation behavior in martensitic steel, Scr. Mater. 178 (2020) 318–323.
[15] M. Yamaguchi, J. Kameda, K. Ebihara, Mobile effect of hydrogen on intergranular decohesion of iron: first-principles calculations, Philos. Mag. 92 (2012) 1349–1368.
[16] I.M. Robertson, P. Sofronis, A. Nagao, M.L. Martin, S. Wang, D.W. Gross, K. E. Nygren, Hydrogen embrittlement understood, Metall. Mater. Trans. A 46 (2015) 2323–2341.
[17] S. Wang, M.L. Martin, I.M. Robertson, P. Sofronis, Effect of hydrogen environment on the separation of Fe grain boundaries, Acta Mater. 107 (2016) 279–288.
[18] M. Rajagopalan, M.A. Tschopp, K.N. Solanki, Grain boundary segregation of interstitial and substitutional impurity atoms in alpha-iron, JOM 66 (2014) 129–138.
[19] S.P. Jung, Y. Kwon, C.S. Lee, B.J. Lee, Influence of hydrogen on the grain boundary crack propagation in bcc iron: A molecular dynamics simulation, Comput. Mater. Sci. 149 (2018) 424–434.
[20] M. Yamaguchi, J. Kameda, Intergranular decohesion induced by mobile hydrogen in iron with and without segregated carbon: first-principles calculations. International Hydrogen Conference (HIC 2012): Hydrogen-Materials Interactions, American Society of Mechanical Engineers (ASME) Press, 2014, pp. 747–755.
[21] D. McLean, A. Maradudin, Grain boundaries in metals, Phys. Today 11 (1958) 35.
[22] M. Paju, H.J. Grabke, Segregation of phosphorus and boron in austenite in Fe...10% Mn...P...B...alloys, Steel Res. 60 (1989) 41–48.
[23] T. Abe, K. Tsukada, H. Tagawa, I. Kozasu, Grain boundary segregation behaviour of phosphorus and carbon under equilibrium and non-equilibrium conditions in austenitic region of steels, ISIJ Int. 30 (1990) 444–450.
[24] G. Miyamoto, A. Goto, N. Takayama, T. Furuhara, Three-dimensional atom probe analysis of boron segregation at austenite grain boundary in a low carbon steel - Effects of boundary misorientation and quenching temperature, Scr. Mater. 154 (2018) 168–171.
[25] T. Ungar, I. Dragomir, A. Revesz, A. Borbely, The contrast factors of dislocations in cubic crystals: the dislocation model of strain anisotropy in practice, J. Appl. Crystallogr. 32 (1999) 992–1002.
[26] G. Ribárik, T. Ungár, J. Gubicza, MWP-fit: a program for multiple whole-profile fitting of diffraction peak profiles by ab initio theoretical functions, J. Appl. Crystallogr. 34 (2001) 298–310.
[27] G. Ribárik, J. Gubicza, T. Ungár, Correlation between strength and microstructure of ball-milled Al...Mg alloys determined by X-ray diffraction, Mater. Sci. Eng. A 387–389 (2004) 343–347.
[28] L. Morsdrof, C.C. Tasan, D. Ponge, D. Raabe, 3D structural and atomic-scale analysis of lath martensite: effect of the transformation sequence, Acta Mater. 95 (2015) 366–377.
[29] Y.J. Li, D. Ponge, P. Choi, D. Raabe, Atomic scale investigation of non-equilibrium segregation of boron in a quenched Mo-free martensitic steel, Ultramicroscopy 159 (2015) 240–247.
[30] J. Takahashi, K. Ishikawa, K. Kawakami, M. Fujioka, N. Kubota, Atomic-scale study on segregation behavior at austenite grain boundaries in boron-and molybdenum-added steels, Acta Mater. 133 (2017) 41–54.
[31] M. Herbig, D. Raabe, Y.J. Li, P. Choi, S. Zaefferer, S. Goto, Atomic-scale quantification of grain boundary segregation in nanocrystalline material, Phys. Rev. Lett. 112 (2014), 126103.
[32] K. Hono, Atom probe microanalysis and nanoscale microstructures in metallic materials, Acta Mater. 47 (1999) 3127–3145.
[33] M. Herbig, M. Kuzmina, C. Haase, R.K.W. Marceau, I. Gutierrez-Urrutia, D. Haley, D.A. Molodov, P. Choi, D. Raabe, Grain boundary segregation in Fe...Mn...C twinning-induced plasticity steels studied by correlative electron backscatter diffraction and atom probe tomography, Acta Mater. 83 (2015) 37–47.
[34] C. Wells, W. Batz, R.F. Mehl, Diffusion coefficient of carbon in austenite, Trans. AIME 188 (1950) 553–560.
[35] A. Shibata, T. Nagoshi, M. Sone, S. Morito, Y. Higo, Evaluation of the block boundary and sub-block boundary strengths of ferrous lath martensite using a micro-bending test, Mater. Sci. Eng. A 527 (2010) 7538–7544.
[36] K. Takasawa, R. Ikeda, N. Ishikawa, R. Ishigaki, Effects of grain size and dislocation density on the susceptibility to high-pressure hydrogen environment embrittlement of high-strength low-alloy steels, Int. J. Hydrog. Energy 37 (2012) 2669–2675.
[37] M.J.G. da Silva, J.L. Cardoso, D.S. Carvalho, L.P.M. Santos, L.F.G. Herculano, H.F. G. de Abreu, J.M. Pardal, The effect of prior austenite grain size on hydrogen embrittlement of Co-containing 18Ni 300 maraging steel, Int. J. Hydrog. Energy 44 (2019) 18606–18615.
[38] M. Yamaguchi, First-principles study on the grain boundary embrittlement of metals by solute segregation: Part I. iron (Fe)-solute (B, C, P, and S) systems, Metall. Mater. Trans. A 42 (2011) 319–329.